IEEE Access
Multidisciplinary | Rapid Review | Open Access Journal

Received September 22, 2018, accepted November 18, 2018, date of publication November 30, 2018,
date of current version December 27, 2018.

Digital Object Identifier 10.1109/ACCESS.2018.2884345

Generalized PFA for Air-Missile Borne Bistatic Forward-Looking Beam-Steering SAR With Accelerations

SHIYANG TANG[1], (Member, IEEE), HUAN DENG[1], PING GUO[2], YACHAO LI[1], AND LINRANG ZHANG[1]

[1]National Laboratory of Radar Signal Processing, Xidian University, Xi'an 710071, China
[2]College of Communication and Information Engineering, Xi'an University of Science and Technology, Xi'an 710054, China

Corresponding author: Yachao Li (ycli@mail.xidian.edu.cn)

This work was supported by the National Natural Science Foundation of China under Grant 61701393, Grant 61601343, Grant 61001211, Grant 61303035, and Grant 61471283.

ABSTRACT For air-missile borne bistatic forward-looking beam-steering synthetic aperture radar (BFLBS-SAR), the receiver platform moves along a curve track due to the existence of accelerations. Besides, transmitting and receiving antenna beams rotate around a certain rotary center during the process of data collection to extend or shorten synthetic aperture time. These characteristics imply that the echo signal suffers serious range–azimuth coupling and aliasing problems of azimuth spectrum. Worse still, the echo process has problems of double-radical sign and high-order terms, which makes the rotary beam center unable to be obtained directly, and thus, the traditional polar formation algorithm (PFA) cannot be applied directly to BFLBS-SAR. To solve these problems, this paper proposes a generalized PFA (GPFA) for air-missile borne BFLBS-SAR. The algorithm uses the equivalent bistatic linear range model first to separate platform acceleration errors. By equating the bistatic mode to the monostatic one, an equivalent rotary center is obtained, and a new azimuth Deramp function is introduced to eliminate aliasing. Then, spectrum utilization and azimuth sampling rate are improved by spectral rotation and interpolation, and the image format is changed. In the azimuth focusing phase, azimuth aliasing is avoided by means of azimuth scaling, which makes azimuth focusing possible eventually. Numerous simulation experiments verify the effectiveness of the proposed GPFA.

INDEX TERMS Bistatic forward-looking beam-steering SAR, generalized polar formation algorithm, equivalent range model, azimuth scaling.

I. INTRODUCTION

With the development of Synthetic Aperture Radar (SAR) imaging technology, it has become a new trend to combine SAR with high-maneuverable platforms such as aircrafts and missiles. Air-missile borne BFLBS-SAR transmits radar beams to the target area by placing the transmitting antenna on the aircraft. The receiver is placed on the missile platform to forward receive echoes of the target, and beams of the transmitting and the receiving antennas are always rotated to extend or shorten synthetic aperture time. This makes it possible to increase azimuth resolution or widen swath width [1], [2]. Such a new imaging detection mode can not only effectively improve the survivability of aircrafts in complex battlefield environment, but also achieve multi-directional silent attack of missiles, which has important military application values.

Changes in azimuth beams of BFLBS-SAR receivers cause the azimuth signal bandwidth to increase sharply [3]–[9]. However, the high three-axis velocity and acceleration of missiles and aircrafts make the azimuth signal bandwidth much larger than the Pulse Repetition Frequency (PRF) so that there exists aliasing in azimuth signals. One way to deal with aliasing is to improve PRF, which will greatly increase the amount of data and make the design of missile-borne SAR systems more complicated [10], [11]. In addition, due to the special geometric configuration of BFLBS-SAR imaging, range models have such problems as double-radical sign and high order terms, and beam directions of transmitting and receiving antennas change with slow time so that it is difficult to determine the rotary center slant range. All of these problems can significantly increase the design difficulty of air-missile borne BFLBS-SAR imaging algorithms.

In view of Bistatic Forward-Looking SAR (BFL-SAR) imaging, the study of [12] proposes a method to simplify the bistatic forward-looking equivalent slant range model to a monostatic SAR slant range model. The BFL-SAR imaging algorithm proposed in [13] and [14] introduces a double-radical sign slant range model by Taylor series expansion, and derives the 2-D spectrum using Method of Series Reversion (MSR). However, this algorithm has low accuracy due to the existence of great accelerations of missile borne platform. In practice, equivalent coefficients are coupled with acceleration parameters so that they cannot be combined with the existing motion compensation algorithm in [15] easily. Frequency-domain bistatic SAR imaging algorithms with good real-time performance mainly include Nonlinear Chirp Scaling Algorithm (NCS) [14], [16] and its extension algorithm [17], [18], Frequency Scaling Algorithm (FSA) [19] and so on. These algorithms make unified compensation for the space-variant phase in the range-Doppler domain based on azimuth shift-invariance of echo data, so the operation efficiency is higher. However, there is a vertical velocity in the air-missile borne BFLBS-SAR imaging, which makes shift-invariance no longer satisfied. Besides, the severe 2-D spectrum coupling and complex space-variant problems caused by large squint angles make these algorithms unable to be applied directly. The polar formation algorithm (PFA) [20]–[25] uses 2-D linear interpolation to resample the spectrum. The existing 2-D separation interpolation algorithms are suitable for parallel processing and can be realized quickly on missile borne platforms. However, it should be noted that the existing algorithms are mainly based on bistatic linear flat-flying configuration and cannot meet the processing requirements of space-variant motion errors introduced by accelerations. In view of Beam-Steering SAR (BS-SAR), [10] and [25] proposes a GPFA that is suitable for monostatic BS-SAR. After 2-D interpolation, the algorithm avoids azimuth aliasing through azimuth scaling. In [23], a GPFA is proposed for bistatic BS-SAR with curve tracks. This algorithm directly expands the Taylor series for the bistatic instantaneous slant range, and derives the 2-D spectrum using MSR. The corresponding process is very complicated, and its 2-D interpolation does not carried out spectrum rotation, so the spectrum utilization is low in the squint imaging mode. Besides, these algorithms are not effective in solving problems that the rotary beam center cannot be determined directly by bistatic forward-looking geometric configurations.

In conclusion, given the above numerous issues in air-missile borne BFLBS-SAR imaging, this paper proposes a new algorithm named GPFA. Compared with the existing studies, this algorithm has the following advantages:

- Compared with traditional PFA, GPFA can meet the imaging application requirements for air-missile borne BFLBS-SAR under multi-work modes.
- GPFA separates the space-variant motion error term caused by accelerations from the bistatic forward-looking non-approximate linear range model through a bistatic equivalent slant range model. This can not only simplify model construction, but also facilitate the subsequent compensation of space-variant motion errors.
- The equivalent rotary center slant range is obtained by equating the bistatic mode to the monostatic one, which enables the establishment of a new azimuth Deramp function to eliminate spectral aliasing.
- Spectrum utilization and azimuth sampling rate are improved by spectrum rotation and 2-D interpolation, and imaging format is also changed.
- The problem of azimuth aliasing is avoided by focusing the image on the azimuth wavenumber domain with the introduction of an azimuth scaling operation. The proposed algorithm only needs PRF to be greater than the azimuth bandwidth and requires a small number of zero padding operations.

This paper is divided into six parts as follows. In Section II, the two equivalent slant range models are introduced. Section III describes the proposed GPFA for air-missile borne BFLBS-SAR in detail. Section IV discusses the computational complexity of the proposed GPFA. Section V further tests the proposed algorithm through simulation experiments. Summations of the whole paper are provided in Section VI.

II. BISTATIC EQUIVALENT SLANT RANGE MODEL FOR BFLBS-SAR

A. EQUIVALENT BISTATIC LINEAR SLANT RANGE MODEL

Assume that the transmitter operates in the sliding spotlight mode, and the corresponding beam rotation center point is denoted as O'_{T-rot}. Also, the receiver operates in the Terrain Observation by Progressive Scans (TOPS) mode, and its beam scanning angle is $\Delta\theta_{R-rot}$. Let θ_T represent the azimuth angle of the transmitter, and t_m be the slow time. When $t_m = 0$, for the receiver and the transmitter, set the positions in the coordinate system to $(0, y_R, H_R)$ and (x_T, y_T, H_T), respectively, the corresponding triaxial velocity vectors to $\left(0, v_{yR}, v_{zR}\right)$ and $\left(v_{xT}, v_{yT}, v_{zT}\right)$, respectively, and the corresponding triaxial acceleration vector of receiver to $\left(a_{xR}, a_{yR}, a_{zR}\right)$. The instantaneous bistatic slant range is expressed in equation (1), as shown at the bottom of the next page.

Based on the bistatic equivalent slant range model proposed by [24], the instantaneous slant range model of the BFLBS-SAR is equivalent to a linear range model with motion error terms. The bistatic equivalent slant range model is

$$\begin{aligned} &R_{eq1}\left(t_m\right) \\ &= R_{LR}\left(t_m\right) + R_{LT}\left(t_m\right) + \sum_{i=2}^{4} A_i\left(x_p, y_p\right) t_m^i \\ &= R_{BL}\left(t_m\right) + \sum_{i=2}^{4} A_i\left(x_p, y_p\right) t_m^i \end{aligned} \tag{2}$$

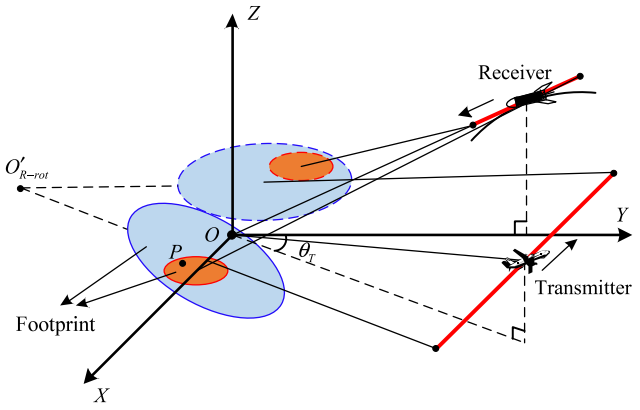

FIGURE 1. Illustration of the geometric configuration of air-missile borne BFLBS-SAR with accelerations.

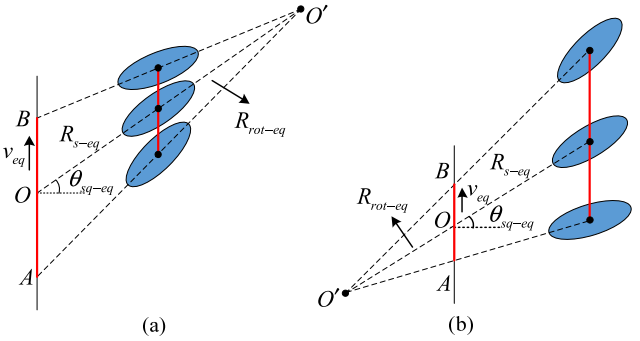

FIGURE 2. Imaging geometry of equivalent monostatic squint BS-SAR. (a) Geometric configuration of sliding spotlight SAR imaging; (b) Geometric configuration of TOPS SAR.

$$R_{BL} = \sqrt{x_p^2 + \left(y_R + v_{Ry}t_m - y_p\right)^2 + \left(H_R + v_{Rz}t_m\right)^2} + \sqrt{\left(x_T + v_{Tx}t_m - x_p\right)^2 + \left(y_T + v_{Ty}t_m - y_p\right)^2 + \left(H_T + v_{Tz}t_m\right)^2} \tag{3}$$

$$A_i = \left(\frac{1}{i!}\frac{\partial^i R_{pro1}}{\partial t_m^i} - \frac{1}{i!}\frac{\partial^i R_{BL}}{\partial t_m^i}\right)\Bigg|_{t_m=0}, \quad i = 2, \cdots, 4 \tag{4}$$

In practical imaging process, the acceleration of the platform will only bring in changes of second and high-order Doppler coefficients instead of the linear Doppler component [24], [26]–[29].

B. EQUIVALENT MONOSTATIC ROTARY SLANT RANGE MODEL

In air-missile BFLBS-SAR imaging, the transmitter works in side-looking modes to transmit radar signals, and its rotary beam center can be directly obtained through geometric configuration. However, the receiver adopts forward-looking modes to receive echo signals, which makes it difficult to determine rotary beam center through its geometric configuration and causes the Deramp function unable to be accurately constructed. In order to determine the rotary beam center in BFLBS-SAR imaging, a modified monostatic hyperbolic range model is used to equilibrate the linear range model $R_{BL}(t_m)$ in equation (3). This makes BFLBS-SAR simplified to the monostatic squint BS-SAR. The geometry configuration of equivalent monostatic BS-SAR is illustrated in Fig. 2 where $R_{s-eq} = R_{BL0}/2$. The figure only lists the sliding spotlight SAR mode (see Fig. 2(a)) and the TOPS SAR mode (see Fig. 2(b)) discussed in this paper [11], [25].

In order to guarantee imaging accuracy, a reasonable approximation of $R_{BL}(t_m)$ is needed before the equivalent process. Besides, considering the influence of high velocity and acceleration of double platforms, higher order terms in the range history need to be involved so as to obtain well-focused SAR images. To achieve these goals, the fifth Taylor series expansion of $R_{BL}(t_m)$ in equation (3) is utilized [29]–[32], and its expression is as follows:

$$R_{BL-5th}(t_m) = R_{BL0} + \sum_{i=1}^{5}\frac{1}{i!}b_i t_m^i \tag{5}$$

where R_{BL0} is the bistatic slant range at $t_m = 0$, and b_i, $i = 1, 2, \cdots, 5$ is the coefficient of Taylor series expansion. The bistatic linear range model $R_{BL}(t_m)$ in (3) can be made equivalent to the following modified instantaneous range model of monostatic BS-SAR:

$$\begin{aligned} R_{eq2}(t_m) &= 2\left(R_{ML}(t_m) + p_1 t_m^3 + p_2 t_m^4 + p_3 t_m^5\right) \\ &= 2\left(\sqrt{\left(\frac{R_{L0}}{2}\cos\theta_{eq}\right)^2 + \left(v_{eq}t_m - \frac{R_{L0}}{2}\sin\theta_{eq}\right)^2} + p_1 t_m^3 + p_2 t_m^4 + p_3 t_m^5\right) \\ &\approx R_{L0} - 2v_{eq}\sin\theta_{eq}t_m + \frac{2v_{eq}^2\cos^2\theta_{eq}t_m^2}{R_{L0}} + \frac{(2p_1 + 2c_3)t_m^3}{6} \\ &\quad + \frac{(2p_2 + 2c_4)t_m^4}{24} + \frac{(2p_3 + 2c_5)t_m^5}{120} \end{aligned} \tag{6}$$

Here, v_{eq}, θ_{eq}, p_1, p_2 and p_3 are the equivalent coefficients to be solved, and $c_i = \partial^i R_{ML}(t_m)/\partial^i t_m$. With equation (5) and

$$R_{pro1}(t_m) = \sqrt{\left(\frac{1}{2}a_{xR}t_m^2 - x_p\right)^2 + \left(y_R + v_{yR}t_m + \frac{1}{2}a_{yR}t_m^2 - y_p\right)^2 + \left(H_R + v_{zR}t_m + \frac{1}{2}a_{zR}t_m^2\right)^2} + \sqrt{\left(x_T + v_{xT}t_m - x_p\right)^2 + \left(y_T + v_{yT}t_m - y_p\right)^2 + \left(H_T + v_{zT}t_m\right)^2} \tag{1}$$

equation (6), the following relationships can be established:

$$\begin{cases} -2v_{eq}\sin\theta_{eq} = b_1 \\ 4v_{eq}^2\cos^2\theta_{eq}/R_{L0} = b_2 \\ 2\left(p_1 + c_3\right) = b_3 \\ 2\left(p_2 + c_4\right) = b_4 \\ 2\left(p_3 + c_5\right) = b_5 \end{cases} \tag{7}$$

Solving equation (7) yields

$$\begin{cases} v_{eq} = \sqrt{b_1^2 + b_2 R_{L0}}/2 \\ \theta_{eq} = \sin^{-1}\left(-b_1/2v_{eq}\right) \\ p_1 = b_3/2 - c_3 \\ p_2 = b_4/2 - c_4 \\ p_3 = b_5/2 - c_5 \end{cases} \tag{8}$$

Taking the TOPS SAR imaging geometry in Fig. 2(b) as an example, and the equivalent rotary center range R_{rot-eq} can be calculated by v_{eq} and θ_{eq} as

$$R_{rot-eq} = -\frac{v_{eq}T_a}{\cos\theta_{eq}\left(\tan\theta_{eq-\max} - \tan\theta_{eq-\min}\right)} \tag{9}$$

$$\begin{cases} \theta_{eq-\min} = \max\left(\sin^{-1}\left(-b_1\left(x_p, y_p\right)/2v_{eq}\right)\right) \\ \theta_{eq-\max} = \min\left(\sin^{-1}\left(-b_1\left(x_p, y_p\right)/2v_{eq}\right)\right) \end{cases} \tag{10}$$

where T_a is the synthetic aperture time, and $\theta_{eq-\max}$ and $\theta_{eq-\min}$ are the maximum and the minimum equivalent squint angles, respectively.

III. GPFA FOR AIR-MISSILE BORNE BFLBS-SAR

Assuming that radar transmits linear frequency modulated signal, the equivalent slant range expression in equation (3) can be used to obtain the wavenumber domain expression of BFLBS-SAR echo signals after pulse compression processing as follows:

$$S_{bf}(k_r, t_m) = W_r(k_r)w_a\left(\frac{t_m - t_{n-eq}}{T_{a-eq}}\right)\exp\left(-jk_r R_{eq1}\left(t_m\right)\right) \tag{11}$$

where k_r is the range wavenumber and $k_r = 2\pi\left(f_r + f_c\right)/c$; t_{n-eq} is the equivalent beam center time; T_{a-eq} is the equivalent synthetic aperture time for which $T_{a-eq} \approx \alpha R_{s-eq}\theta_{BW}/(v_{eq}\cos\theta_{n-eq})$ if $\alpha = R_{rot-eq}/(R_{rot-eq} + R_{s-eq})$; θ_{n-eq} is the equivalent rotating angle of the target point (TP) P relative to the rotary center; θ_{BW} is the beam width of the receiver; $W_r(\cdot)$ is the frequency domain form of the range window function; $w_a(\cdot)$ is the azimuth window function. It can be seen from equation (11) that the phase history expression of BS-SAR is the same as the traditional stripe mode. The difference between them lies in the azimuth window function, which indicates that the interval of the BS-SAR 2-D spectrum is different from that of the strip mode [10], [11].

A. SPACE-INVARIANT MOTION ERROR COMPENSATION AND AZIMUTH DERAMP

From the equivalent slant range model in equation (2), it can be observed that the instantaneous slant range model of BFLBS-SAR includes a uniform linear slant range model and a space-variant motion error term caused by accelerations. Here, the motion error term can cause changes of Doppler coefficients, resulting in compression or broadening of the azimuth spectrum [26], [27]. In addition, as the direction of the beam changes with slow time, the azimuth bandwidth of the echo signal will experience a sharp increase and is usually much larger than the PRF, which makes the azimuth spectrum aliased. As a result, the traditional Deramp function in the spotlight mode cannot be used to process the whole scene [20]–[22]. Fig. 3 is a time-frequency map of the Deramp processing in BFLBS-SAR on squint mode [11], [25]. The PRF is only slightly larger than the azimuth instantaneous bandwidth B_{inst} and less than the azimuth signal bandwidth B_a of the original echo signal, and the signal spectrum is aliased. After multiplied by the azimuth Deramp function and the space-invariant motion error compensation function, the azimuth spectrum is compressed and the scene is coarsely focused, but there is still aliasing in the scene.

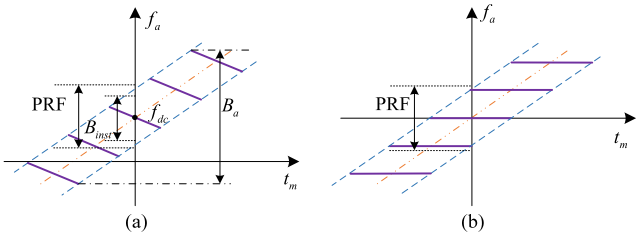

FIGURE 3. Time-frequency map of azimuth Deramp processing. (a) The time-frequency map of azimuth signal before azimuth Deramp processing. (b) The time-frequency map of azimuth signal after azimuth Deramp processing.

Taking the scene center as the reference point, the rough compensation function of space-invariant motion errors is constructed and multiplied by the distorted signal spectrum. The purpose of this operation is to eliminate space-invariant components in the motion error term and make the spectrum approximate to that of the conventional linear model. After this, Deramp processing is achieved by multiplying the recovered signal spectrum with the newly constructed azimuth Deramp function. The motion error rough compensation function and the azimuth Deramp function are

$$H_{ACC} = \exp\left(jk_r\sum_{i=2}^{4}A_{i0}\left(0,0\right)t_m^i\right) \tag{12}$$

$$H_{Drmp} = \exp\left(j2k_r\left(R_{rot-eq}\sqrt{1+\left(\frac{v_{eq}t_m}{R_{rot-eq}}\right)^2 - \frac{2v_{eq}\sin\theta_{eq}t_m}{R_{rot-eq}}} + p_1t_m^3 + p_2t_m^4 + p_3t_m^5 + \left(\frac{R_{BL0}}{2} - R_{rot-eq}\right)\right)\right) \tag{13}$$

After compensation of the Deramp function, the signal can be expressed as

$$\begin{aligned} &S_{drmp}\left(k_r, t_m\right) \\ &= W_r\left(k_r\right) w_a\left(t_m\right) \exp\left(-jk_r\left(R_{BL}\left(t_m\right) - R_{BLs}\left(t_m\right)\right.\right. \\ &\quad \left.\left. + \sum_{i=2}^{4} D_i\left(x_p, y_p\right) t_m^i\right)\right) \\ &\quad \times \exp\left(-jk_r\left(R_{BLs}\left(t_m\right)\right.\right. \\ &\quad \left.\left. - 2\left(\begin{array}{l} R_{rot-eq}\sqrt{1+\left(\dfrac{v_{eq}t_m}{R_{rot-eq}}\right)^2 - \dfrac{2v_{eq}\sin\theta_{eq}t_m}{R_{rot-eq}}} \\ +p_1 t_m^3 + p_2 t_m^4 + p_3 t_m^5 + \left(\dfrac{R_{BL0}}{2} - R_{rot-eq}\right) \end{array}\right)\right)\right) \end{aligned} \tag{14}$$

$$D_i\left(x_p, y_p\right) = A_i\left(x_p, y_p\right) + A_{i0}\left(0, 0\right) \tag{15}$$

where $R_{BLs}\left(t_m\right)$ is the instantaneous slant range of $R_{BL}\left(t_m\right)$ at the scene center $x_p = 0, y_p = 0$.

B. SPECTRAL ROTATION AND INTERPOLATION

In order to improve spectrum utilization, the spectrum is rotated and interpolated, and the interpolation kernel functions k_x' and k_y' are as follows [21]–[23]:

$$\begin{cases} k_x' = k_x \cos\varphi_{bis} + k_y \sin\varphi_{bis} \\ k_y' = -k_x \sin\varphi_{bis} + k_y \cos\varphi_{bis} \end{cases} \tag{16}$$

$$\begin{cases} k_x = k_r \Gamma_x\left(t_m\right) \\ k_y = k_r \Gamma_y\left(t_m\right) \end{cases} \tag{17}$$

$$\begin{cases} \Gamma_x = -\left(x_T + v_{xT}t_m\right)/R_{T0} = -\cos\psi_T \sin\theta_T \\ \Gamma_y = -\left(\left(y_R + v_{yR}t_m\right)/R_{R0} + \left(y_T + v_{yT}t_m\right)/R_{T0}\right) \\ \quad = -\left(\cos\psi_R + \cos\psi_T \cos\theta_T\right) \end{cases} \tag{18}$$

where ψ_T and θ_T are the instantaneous grazing angle and the azimuth angle of the transmitter, respectively, while ψ_R is the counterparts of the receiver. The expression of the bistatic angle φ_{bis} is

$$\varphi_{bis} = \tan^{-1}\left(\frac{\cos\psi_R + \cos\psi_T \cos\theta_T}{\cos\psi_T \sin\theta_T}\right) \tag{19}$$

The range wavenumber k_r^* and the azimuth time t_m^* after interpolation can be obtained from equation (16), equation (17) and equation (18). Since there is a double-radical sign in the expressions, the MSR is required [23], [24], [30]. In the process of 2-D spectral interpolation, the azimuth signal can be up-sampled by adjusting the width of $\Delta k_x'$ and $\Delta k_y'$ as well as the number of the range and azimuth points. By doing so, the range and the azimuth sampling rate can be equivalently lifted, and azimuth spectrum de-aliasing can be achieved.

Substitute equation (10) and equation (11) into equation (8), and the signal expression after spectral rotation and interpolation can be obtained:

$$\begin{aligned} &S_{drmp}\left(k_x', k_y'\right) \\ &= W_r\left(k_x'\right) W_a\left(k_y'\right) \\ &\quad \times \exp\left(-j\left(\Delta_{10}\left(k_x' - k_{xc}'\right) + \Delta_{11}k_y' + \Delta_{21}k_y'^2\right)\right) \\ &\quad \times \exp\left(j2k_r^*\left(\begin{array}{l} R_{rot-eq}\sqrt{1+\left(\dfrac{v_{eq}t_m^*}{R_{rot-eq}}\right)^2 - 2\dfrac{v_{eq}\sin\theta_{eq}t_m^*}{R_{rot-eq}}} \\ -\dfrac{R_{BLs}\left(t_m^*\right)}{2} + p_1 t_m^{*3} + p_2 t_m^{*4} + p_3 t_m^{*5} \\ +\left(\dfrac{R_{BL0}}{2} - R_{rot-eq}\right) \end{array}\right)\right) \\ &\quad \times \exp\left(-jk_r^* \sum_{i=2}^{4} D_i\left(x_p, y_p\right) t_m^{*i}\right) \end{aligned} \tag{20}$$

$$k_r^* = \left(\cos\varphi_{bis}k_x' - \sin\varphi_{bis}k_y'\right)/\cos\psi_T \sin\theta_T \tag{21}$$

In equation (20), the first exponential term is the focus term of the target and the wavefront bending phase. Δ_{10}, Δ_{11} and Δ_{21} are the Taylor expansion coefficients, and their expressions are the same as those in the conventional bistatic spotlight mode and derived in existing literatures [20]–[24]. The second exponential term is the high-order term of the range wavenumber and the azimuth wavenumber generated by the azimuth Deramp. It can lead to 2-D defocus, but is independent of the target position, so that uniform compensation can be performed. The third exponential term is the residual space-variant motion error and will cause azimuth defocus.

Since the third and the fourth exponential terms in equation (20) are independent of the specific target position, they can be uniformly compensated, and the corresponding compensation function is

$$\begin{aligned} &H_{comp} \\ &= \exp\left(-j2k_r^*\left(\begin{array}{l} R_{rot-eq}\sqrt{1+\left(\dfrac{v_{eq}t_m^*}{R_{rot-eq}}\right)^2 - \dfrac{2v_{eq}\sin\theta_{eq}t_m^*}{R_{rot-eq}}} \\ -\dfrac{R_{BLs}}{2} + pt_m^{*3} + qt_m^{*4} + \left(\dfrac{R_{BL0}}{2} - R_{rot-eq}\right) \end{array}\right)\right) \end{aligned} \tag{22}$$

The range IFFT is applied to the signal after space-invariant phase compensation, and the range-focused signal is obtained as follows:

$$\begin{aligned} &S_{bf}\left(X, k_y'\right) \\ &\quad = \mathrm{Sinc}\left(X - \Delta_{10}\right) W_a\left(k_y'\right) \exp\left(-j\Delta_{11}k_y'\right) \\ &\qquad \times \exp\left(-j\left(\Delta_{21}k_y'^2 + k_r^* \sum_{i=2}^{4} D_i\left(x_p, y_p\right) t_m^{*i}\right)\right) \end{aligned} \tag{23}$$

To improve the efficiency of residual motion error compensation, let $k_x' = k_{xc}'$, k_{xc}' equal the value of k_x' when $k_{rc} = 2\pi f_c/c$, $t_m = 0$.

C. AZIMUTH SCALING AND IMAGE FOCUSING

The signals in equation (23) still have aliasing in the azimuth spatial domain, and if the azimuth IFFT is conducted directly, the image cannot be focused well. In order to avoid azimuth aliasing, the azimuth scaling function is introduced into azimuth focusing [10], and it is constructed as

$$H_{scl-eq} = \exp\left(-jk_y'^2 R_{scl}\left(R_{rot-eq} - R_{BL0}/2\right)/\left(2k_{xc}' R_{rot-eq}\right)\right) \tag{24}$$

where R_{scl} is the scaling distance, and it can take $R_{scl} = R_{BL0}/2$. Multiplying equation (23) by equation (24) and conducting azimuth FFT, the azimuth spatial expression can be obtained:

$$\begin{aligned} &S_{bf}(X, Y) \\ &= \mathrm{Sinc}(X - \Delta_{10})\, w_a\left(k_y'\right) \\ &\quad \times \exp\left(-j\frac{k_{xc}' R_{rot-eq}}{2R_{scl}\left(R_{rot-eq} - R_{BL0}/2\right)}(Y - \Delta_{11})^2\right) \\ &\quad \times \exp\left(j\phi_{temp}(Y)\right) \end{aligned} \tag{25}$$

Here, $\phi_{temp}(Y)$ is the result of the second exponential term in equation (23) after azimuth FFT. By constructing the azimuth Deramp function to compensate the second-order phase in (25), the phase compensation function is

$$H_{scl-comp} = \exp\left(-j\frac{k_{xc}' R_{rot-eq}}{2R_{scl}\left(R_{rot-eq} - R_{BL0}/2\right)}X^2\right) \tag{26}$$

Multiply equation (23) by equation (24) and conduct FFT. Coarse-focus SAR images in the spatial-wavenumber domain can be obtained:

$$\begin{aligned} &S_{bf}\left(X, k_y'\right) \\ &= \mathrm{Sinc}(X - \Delta_{10}) \\ &\quad \times \mathrm{Sinc}\left(k_y' + \frac{k_{xc}' R_{rot-eq}\Delta_{11}}{R_{scl}\left(R_{rot-eq} - R_{BL0}/2\right)}\right) \\ &\quad \times \exp\left(-j\frac{k_{xc}' R_{rot-eq}}{2R_{scl}\left(R_{rot-eq} - R_{BL0}/2\right)}\Delta_{11}^2\right) \\ &\quad \times \exp\left(-j\left(\Delta_{21}k_y'^2 + k_r^*\sum_{i=2}^{4} D_i\left(x_p, y_p\right) t_m^{*i}\right)\right) \end{aligned} \tag{27}$$

Here, the first exponential term is independent of image focus and can be ignored; the second term is the residual space-variant phase error, and it can be compensated through the joint compensation method of image distortion and space-variant phase error. There exist numerous studies in the existing literature [2], [26], and thus detailed analysis is omitted in this study. The space-variant phase error compensation function is

$$H_{comp-var} = \exp\left(-j\left(\Delta_{21}k_y'^2 + k_r^*\sum_{i=2}^{4} D_i\left(x_p, y_p\right) t_m^{*i}\right)\right) \tag{28}$$

Multiply equation (27) by equation (28), and there exists

$$\begin{aligned} S_{bf}(X, Y) &= \mathrm{Sinc}(X - \Delta_{10}) \\ &\quad \times \mathrm{Sinc}\left(k_y' + \frac{k_{xc}' R_{rot-eq}\Delta_{11}}{R_{scl}\left(R_{rot-eq} - R_{L0}/2\right)}\right) \end{aligned} \tag{29}$$

Based on equation (29), it can be observed that the image has been well focused. However, there still exists a certain degree of geometric distortions which require corresponding correction. The image geometric distortion correction mapping function is

$$\begin{cases} X_{img} = \Delta_{10} \\ Y_{img} = -\dfrac{k_{xc}' R_{rot-eq}\Delta_{11}}{R_{scl}\left(R_{rot-eq} - R_{L0}/2\right)} \end{cases} \tag{30}$$

Using the mapping relationship in equation (30) to correct the geometric distortion, an undistorted SAR image can be obtained [33], [34].

The process of the GPFA can be better illustrated by the flowchart in Fig. 4.

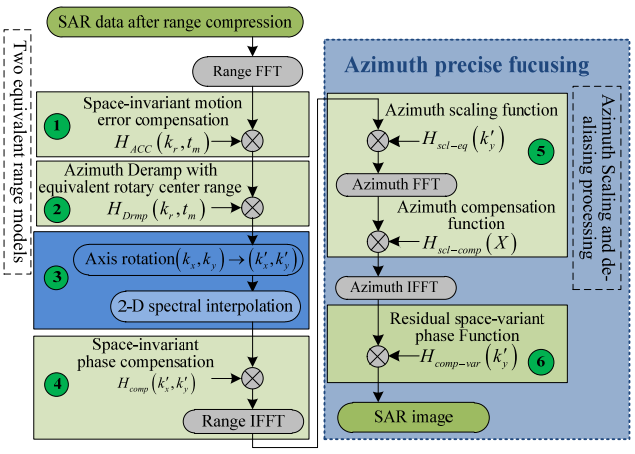

FIGURE 4. Flowchart of proposed GPFA.

IV. COMPUTATION ANALYSIS

As can be seen from the flowchart in Fig. 4, GPFA mainly includes two range FFT/IFFT operations, two azimuth FFT/IFFT operation, five complex multiplications and one two-dimensional interpolation. If the interpolated 8-point sinc function is adopted, and the range and the azimuth sampling points of the data are N_r and N_a, respectively. Then the total computation budget of the algorithm in non-parallel sequential execution is about

$$C = 2N_aN_r\log_2 N_r + 2N_rN_a\log_2 N_a + 21N_rN_a \tag{31}$$

To facilitate the analysis of time complexity, assume that the number of range sampling units is N_a, and the number of azimuth pulses is N_a. As shown in Fig. 4, the time complexity of the proposed algorithm is $\left(4N_a^2 \log_2 N_a + 21N_a^2\right)$ whose magnitude order is $O\left(N_a^2 \log_2 N_a\right)$. Similarly, it can be derived that the time complexity of the traditional PFA is $\left(3N_a^2 \log_2 N_a + 18N_a^2\right)$ with a magnitude order of $O\left(N_a^2 \log_2 N_a\right)$. That is, the magnitude order of time complexity of the proposed algorithm is equivalent to that of the traditional PFA.

V. SIMULATION AND RESULTS

To verify the effectiveness of the GPFA proposed in this paper, consider the three-axis velocity and acceleration of the platform. The corresponding specific simulation parameters are shown in Table 1.

TABLE 1. Equivalent slanting range accuracy simulation parameters.

Parameter	Value	
	Transmitter	Receiver
Work mode	Sliding spotlight/Sliding spotlight	TOPS/Spotlight
Location	(11.12,19.24,5.95)km	(7.5,0,12.99)km
Velocity	(500,-50,0)m/s	(0,-1000,-268)m/s
Acceleration	$(0,0,0)\ \mathrm{m/s^2}$	$(10,5,-5)\ \mathrm{m/s^2}$
Beam scanning angle	\	15° /0°
Rotary center slant range	23km/23km	\
Beam width	10°	5°
Carrier frequency	17GHz	
PRF	2500Hz	
Pulse bandwidth	200MHz	
Sampling frequency	250MHz	
Bistatic angle	70.13°	
Azimuth time	0.82s	

The simulation experiment is divided into three parts to analyze the algorithm better. In the first part, the accuracy of the proposed equivalent slant range model and the approximation of the residual space-variant motion error in (23) are verified through simulation experiments, which indicates that they can meet the imaging requirements of air-missile borne BFLBS-SAR. In the second part, the imaging results of the proposed Deramp function are compared with those of the traditional Deramp function in the reference algorithm [24] to highlight the accuracy of the proposed Deramp operation. The third part discusses imaging results of the TPs with the transmitter and the receiver in different work modes including sliding spotlight, spotlight and TOPS. This manifests that the proposed GPFA can meet the requirements of various work modes.

A. PART I: ANALYSIS OF APPROXIMATION ERROR

In the derivation of the proposed algorithm, (3) and (6) conduct equivalence and approximation of the slant range model

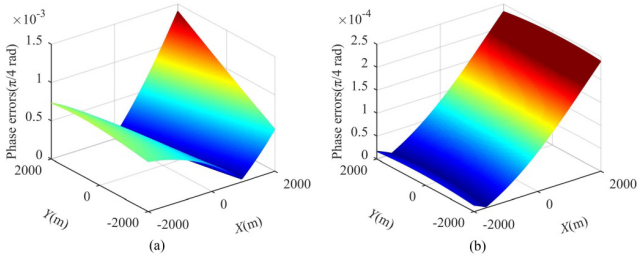

FIGURE 5. Phase error analysis. (a) Phase error of equivalent bistatic linear slant range model $R_{eq1}(t_m)$. (b) Phase error of equivalent monostatic slant range model $R_{eq2}(t_m)$.

respectively. In order to verify the accuracy of such approximation, parameters in Table 1 are used for the simulation experiment with the scene width of 4km×4km. Fig. 5 shows the phase error results of the two slant range models. The phase error introduced by the equivalent bistatic linear slant range model $R_{eq1}(t_m)$ is shown in Fig. 5(a). This figure shows that the phase error is far less than $\pi/4$ and thus will not affect imaging quality. Fig. 5(b) is the phase error result introduced by the approximation of the equivalent monostatic slant range model $R_{eq2}(t_m)$. Similar to Fig. 5(a), it can be seen that the phase error is far less than $\pi/4$, so its effect on imaging can be ignored.

In order to improve the efficiency of space-variant phase error compensation, the value of k_x' in (28) is approximated by k_{xc}', which will introduce range migration and range phase errors. Fig. 6(a) presents the range migration error results corresponding to the edge points of the scene. The maximum range migration error caused by approximation is 0.12m. When the resolution of the range bin is greater than 0.48m, such an approximation will not bring in migration of range bin. Fig. 6(b) is the results of range phase errors. It can be seen that the range phase error is 0.03 times of $\pi/4$, which is far less than $\pi/4$ and will not cause range defocusing. Based on the above analysis, it can be concluded that the model accuracy of the proposed algorithm is high enough. Therefore, this algorithm will not affect 2-D focusing, and can meet the application requirements of BFLBS-SAR imaging.

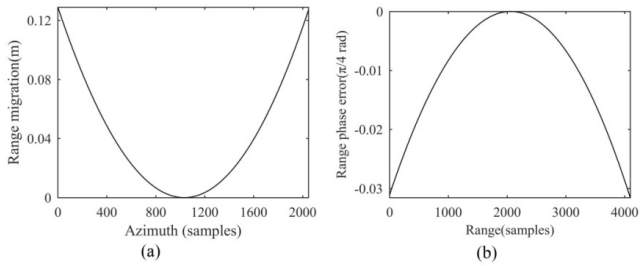

FIGURE 6. Range migration and range phase error introduced by the approximation of k_x. (a) Range migration error. (b) Range phase error.

B. PART II: VALIDITY ANALYSIS OF AZIMUTH DERAMP AND AZIMUTH SCALE

For BFLBS-SAR imaging, its rotary beam center changes with slow time, resulting in changes in Doppler parameters.

Therefore, the traditional azimuth Deramp function is unable to meet imaging requirements. To verify the effectiveness of the proposed azimuth Deramp function, simulation experiments are conducted with the parameters in Table 1, and the corresponding simulation layout is shown in Fig. 7. In the XOY plane, a 21×1 dot matrix is arranged along an isometric line where the scene center point (0,0,0) is located, and the maximum X-direction width of the dot matrix is 2.5km. The transmitter operates in the sliding spotlight mode, while the receiver operates in the TOPS mode.

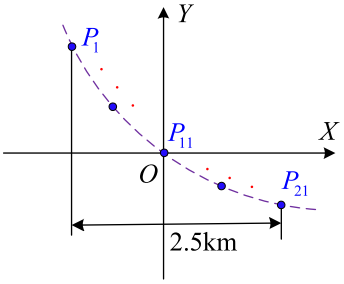

FIGURE 7. Diagram of simulation layout.

Fig. 8(a) shows the imaging results obtained by using the traditional Deramp function given in [24]. As the beam changes with slow time, Doppler parameters of scene edge points have large space-variance. This makes the scene edge points still have large first, second and high order residual terms when the traditional Deramp method is used, and the image edge unable to be focused. Fig. 8(b) presents the imaging results of the Deramp function proposed in this paper. Since the influence of beam-steering on Doppler parameters is considered, the space-variant phase error of the whole scene is well compensated, and the central points and the edge points are well focused. This establishes the validity of the azimuth Deramp function constructed based on the equivalent rotary beam center.

For BFLBS-SAR imaging, the scanning of the receiver beam extends the imaging scene so that the azimuth bandwidth of the echo signal is larger than PRF, which results in spectrum aliasing in the azimuth spatial domain as shown in Fig. 9(a). In order to solve the problem of spectrum aliasing, this paper changes the azimuth signal from spatial domain to wavenumber domain by introducing an azimuth scaling function. At this point, the time-frequency curve of the signal is no longer aliased, and the image can be well focused in the azimuth wavenumber domain, as shown in Fig. 9(b). This verifies the effectiveness of the azimuth scaling method for aliasing.

C. PART III: ANALYSIS OF IMAGING RESULTS IN MULTI-WORK MODES

In order to verify the adaptability of the proposed GPFA to imaging in multi-work modes, this part discusses the imaging results of TPs in two modes, namely, sliding spotlight-TOPS and sliding spotlight-spotlight. The simulation parameters

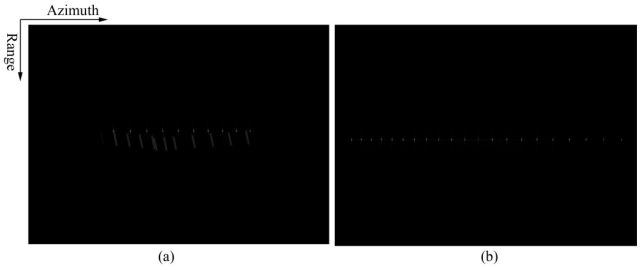

FIGURE 8. Comparison of results using different azimuth Deramp method. (a) Imaging results of traditional Deramp method. (b) Imaging results of the proposed Deramp method.

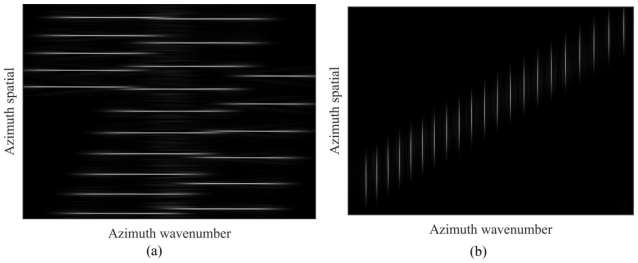

FIGURE 9. Azimuth aliasing analysis. (a) Before de-aliasing. (b) After de-aliasing by using azimuth scaling.

used are shown in Table 1. A 3×1 dot-matrix is arranged on the isometric line where the scene center point is located, and the X-direction width of the scene is 2.5 km. Let TP1, TP2, TP3 represent the left, the middle and the right TP, respectively.

Fig. 10 shows the azimuth profile results of the three TPs in the sliding spotlight-TOPS mode. According to the results in the figure, the main lobe and the side lobe are separated obviously, and the center point and the edge point of the scene are well focused. Fig.11 shows the contour plot results of the three TPs obtained by the reference algorithm proposed in [24]. Experiment results indicate that the reference algorithm is significantly defocused. Fig. 12 shows the contour plots of the three TPs processed by the proposed GPFA. It can be seen from the results that both the center and the edge points of the scene are well focused, presenting the shape of ''cross''. Table 2 summarizes the imaging performance parameters of the three TPs. In this table, PSLR is the peak sidelobe ratio, while ISLR is the integral sidelobe ratio. The corresponding theoretical values of PSLR and ISLR are -13.26dB and -9.8dB, respectively. The expression of PSLR and ISLR are

$$\begin{cases} PSLR = 10\lg \dfrac{P_{sidelobe}}{P_{mainlobe}} \\ ISLR = 10\lg \dfrac{E_{sidelobe}}{E_{mainlobe}} \end{cases} \tag{32}$$

where $P_{sidelobe}$ and $P_{mainlobe}$ represent the amplitude of the sidelobe and the mainlobe, respectively, and $E_{sidelobe}$ and $E_{mainlobe}$ represent the energy of the sidelobe and the mainlobe, respectively.

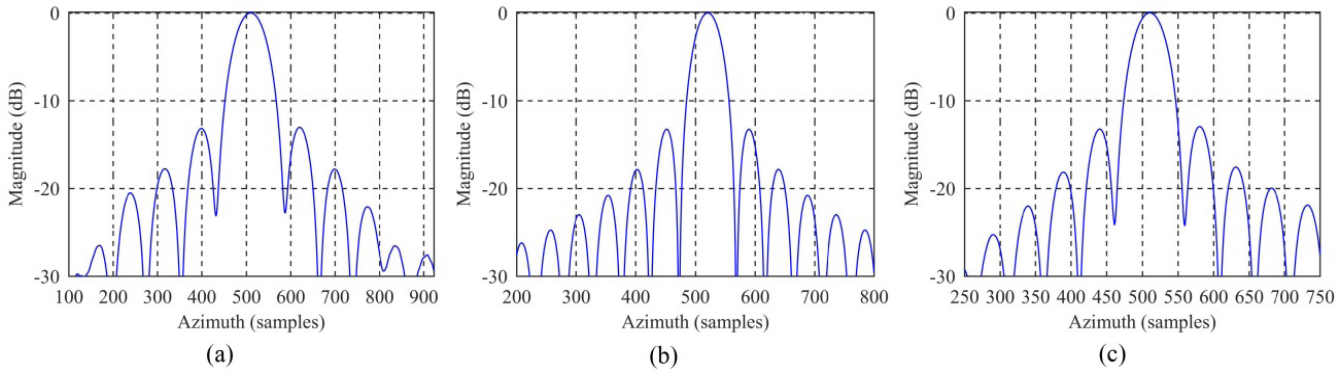

FIGURE 10. Azimuth profile results of sliding spotlight-TOPS SAR processed by GPFA. (a) Azimuth profile of TP1. (b) Azimuth profile of TP2. (c) Azimuth profile of TP3.

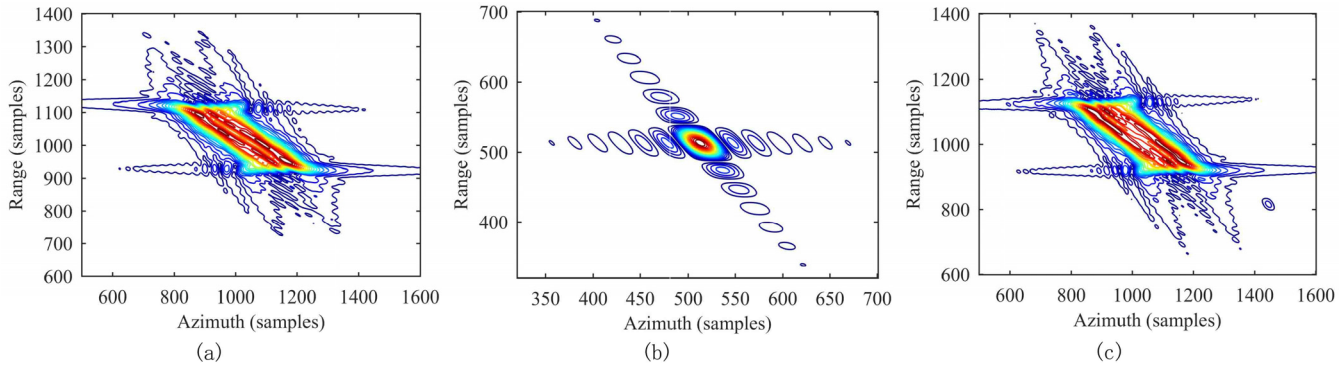

FIGURE 11. Contour plot results of sliding spotlight-TOPS SAR processed by referenced algorithm. (a) Contour plot of TP1. (b) Contour plot of TP2. (c) Contour plot of TP3.

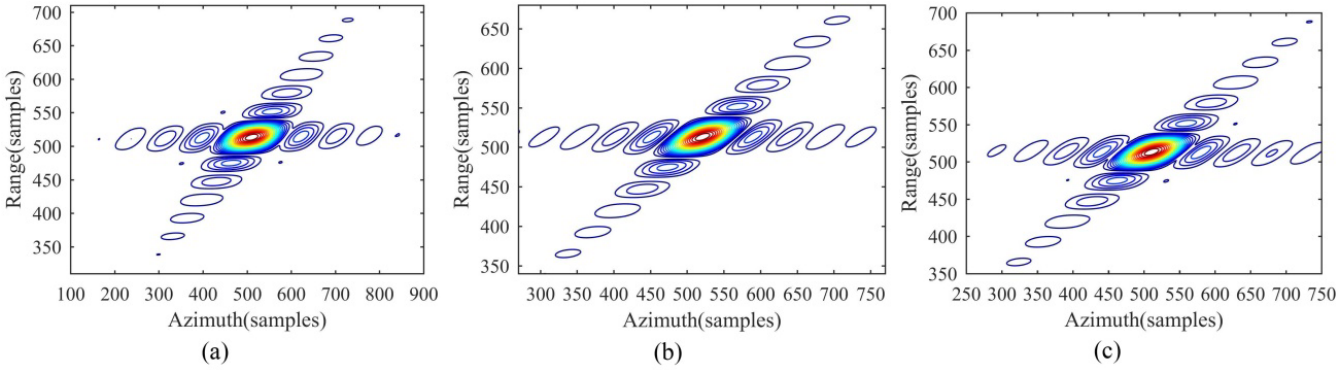

FIGURE 12. Contour plot results of sliding spotlight-TOPS SAR processed by GPFA. (a) Contour plot of TP1. (b) Contour plot of TP2. (c) Contour plot of TP3.

It can be observed that the imaging performances of both the center and the edge points are close to their theoretical values. This further proves that the GPFA proposed in this paper can meet the application requirements of bistatic sliding spotlight-TOPS SAR imaging.

In order to verify the applicability of the proposed GPFA to sliding spotlight-spotlight SAR imaging, simulation experiments are performed using the parameters in Table 1. A 3×1 dot-matrix is arranged on the isometric line where the scene center point is located, and the X-direction width of the scene is 1 km.

Fig. 13 shows the azimuth profile imaging results of the three TPs in the sliding spotlight-spotlight mode. It can be seen from the results that the main lobe and the side lobe are clearly separated, and the center point and the edge point are well focused. Fig.14 shows the contour plot results of the three TPs obtained by the reference algorithm proposed in [24]. Experiment results indicate that the reference

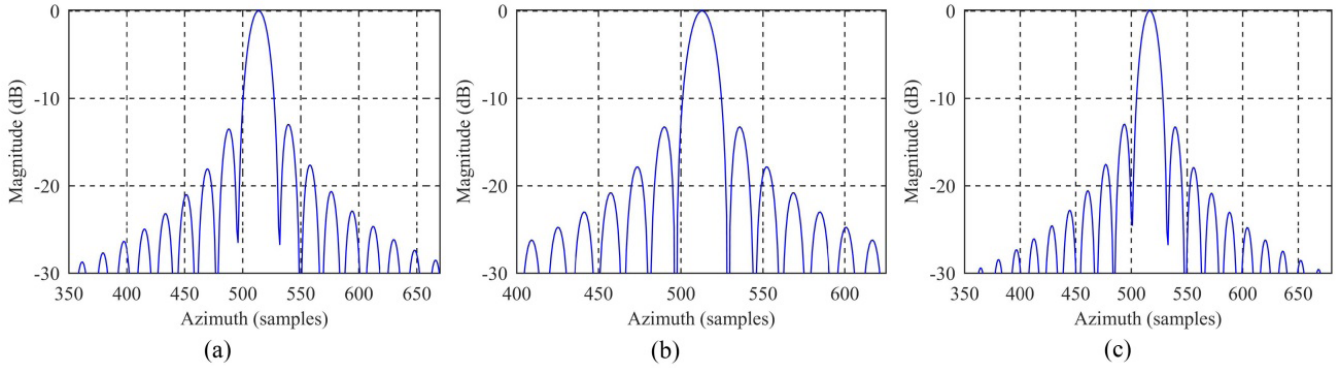

FIGURE 13. Azimuth profile results of sliding spotlight-spotlight SAR processed by GPFA. (a) Azimuth profile of TP1. (b) Azimuth profile of TP2. (c) Azimuth profile of TP3.

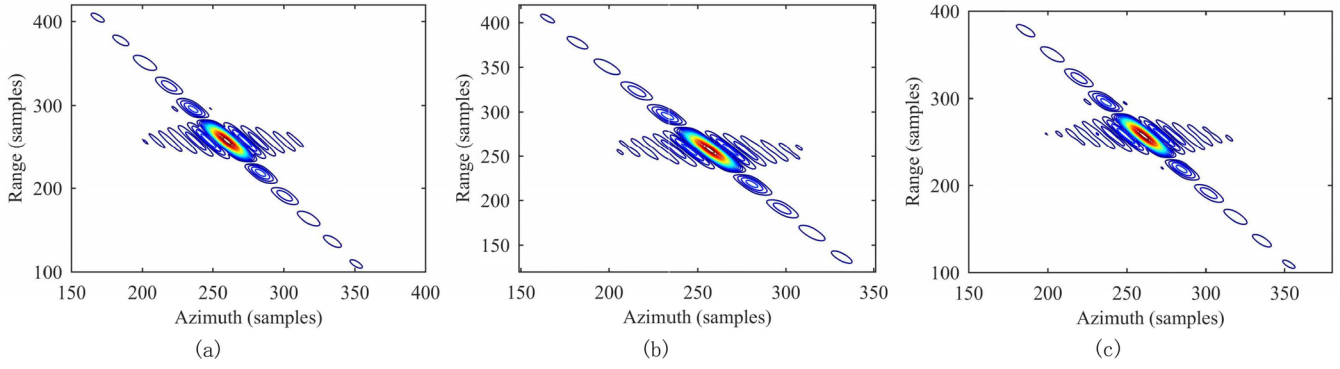

FIGURE 14. Azimuth profile results of sliding spotlight-spotlight SAR processed by referenced algorithm. (a) Contour plot of TP1. (b) Contour plot of TP2. (c) Contour plot of TP3.

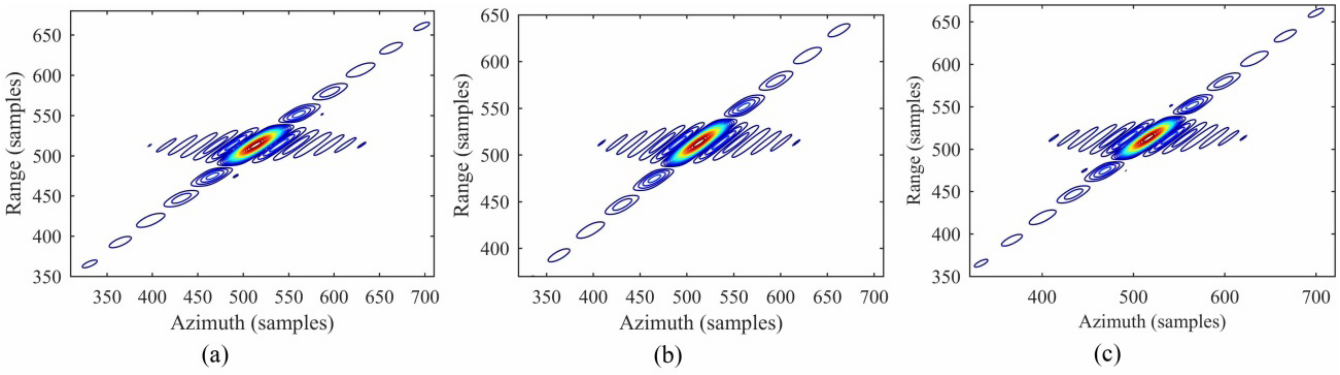

FIGURE 15. Contour plot results of sliding spotlight-spotlight SAR processed by GPFA. (a) Contour plot of TP1. (b) Contour plot of TP2. (c) Contour plot of TP3.

algorithm is focused well. Fig. 15 shows the contour plots of the three TPs, and it manifests that both the center point and the edge point are well focused, presenting the shape of ''cross''. In Table 3, imaging performance parameters of the three TPs are calculated. According to these results, the imaging performances of both the center point and the edge point are close to the corresponding theoretical values, which further verify that the proposed GPFA can meet the application requirements of bistatic sliding spotlight-spotlight SAR imaging.

In summary, it can be concluded that the proposed GPFA can meet the imaging application requirements of multi-work modes such as sliding spotlight-TOPS SAR and sliding spotlight-spotlight SAR. However, the traditional PFA in [24] only can meet the application requirements of sliding spotlight-spotlight SAR.

TABLE 2. Imaging performance results.

Parameters	TP1	TP2	TP3
Azimuth Resolution(m)	2.78	1.75	1.79
PSLR(dB)	-13.05	-13.25	-12.95
ISLR(dB)	-10.61	-10.57	-10.40

TABLE 3. Imaging performance results.

Parameters	TP1	TP2	TP3
Azimuth Resolution(m)	0.68	0.64	0.6
PSLR(dB)	-13.00	-13.26	-12.97
ISLR(dB)	-10.50	-10.51	-10.37

VI. CONCLUSION

As a novel SAR mode that applies the bistatic forward-looking SAR imaging system to the air-missile borne platform, the air-missile borne BFLBS-SAR can yield 2-D imaging and autonomous guidance at the diving stage. In this paper, an algorithm named GPFA is proposed to solve various problems in air-missile borne BFLBS-SAR imaging. This algorithm takes into account the effect of space-variant Doppler parameters caused by rotary beam center, and puts forward an azimuth Deramp function based on the equivalent rotation center to make the image coarsely focused. Furthermore, the space-variant phase error caused by the high acceleration of the missile-borne platform is reduced through the compensation of space-invariant motion errors, and the image format is changed by spectral rotation and interpolation. After subsequent space-invariant phase compensation, the signal is focused on the azimuth spatial domain by means of azimuth scaling method. This solves the problem of image aliasing caused by traditional matching filtering operations. Finally, the scene is well focused with the compensation of residual motion error term and wavefront bending term. Compared with traditional PFA algorithms, this algorithm can meet the imaging application requirements under multi-work modes. In addition, PRF only needs to be larger than the azimuth instantaneous bandwidth and smaller than the azimuth signal bandwidth, which reduces the design complexity of the parameters of the BFLBS-SAR system. Therefore, the proposed algorithm can better solve such issues as imaging accuracy, space-variant motion error compensation and image aliasing in air-missile borne BFLBS-SAR imaging, and provides an effective solution for this new SAR imaging mode.

REFERENCES

[1] J. Mittermayer, R. Lord, and E. Boerner, "Sliding spotlight SAR processing for TerraSAR-X using a new formulation of the extended chirp scaling algorithm," in *Proc. IEEE IGARSS*, Toulouse, France, Jul. 2003, pp. 1462–1464.

[2] P. Prats, R. Scheiber, J. Mittermayer, A. Meta, and A. Moreira, "Processing of sliding spotlight and TOPS SAR data using baseband azimuth scaling," *IEEE Trans. Geosci. Remote Sens.*, vol. 48, no. 2, pp. 770–780, Feb. 2010.

[3] G. C. Sun *et al.*, "Multichannel full-aperture azimuth processing for beam steering SAR," *IEEE Trans. Geosci. Remote Sens.*, vol. 51, no. 9, pp. 4761–4778, Sep. 2013.

[4] G. Sun, M. Xing, Y. Wang, Y. Wu, Y. Wu, and Z. Bao, "Sliding spotlight and TOPS SAR data processing without subaperture," *IEEE Geosci. Remote Sens. Lett.*, vol. 8, no. 6, pp. 1036–1040, Nov. 2011.

[5] W. Xu, P. Huang, Y. Deng, J. Sun, and X. Shang, "An efficient approach with scaling factors for tops-mode SAR data focusing," *IEEE Geosci. Remote Sens. Lett.*, vol. 8, no. 5, pp. 929–933, Sep. 2011.

[6] P. Guo, S. Tang, L. Zhang, and G.-C. Sun, "Improved focusing approach for highly squinted beam steering SAR," *IET Radar, Sonar Navigat.*, vol. 10, no. 8, pp. 1394–1399, Oct. 2016.

[7] Y. Wu, G.-C. Sun, M. Xing, and Z. Bao, "Novel signal processing approach for squint beam-steering SAR (BS-SAR)," *J. Xidian Univ.*, vol. 41, no. 3, pp. 56–62, Jun. 2014.

[8] S. Tang *et al.*, "A novel approach for highly squinted beam steering SAR data focusing," in *Proc. IEEE IGARSS*, Beijing, China, Jul. 2016, pp. 995–998.

[9] J. Chen, G.-C. Sun, M. Xing, J. Yang, Z. Li, and G. Jing, "A two-dimensional beam-steering method to simultaneously consider Doppler centroid and ground observation in GEOSAR," *IEEE J. Sel. Topics Appl. Earth Observ. Remote Sens.*, vol. 10, no. 1, pp. 161–167, Jan. 2017.

[10] G.-C. Sun, M. Xing, X.-G. Xia, Y. Wu, and Z. Bao, "Beam steering SAR data processing by a generalized PFA," *IEEE Trans. Geosci. Remote Sens.*, vol. 51, no. 8, pp. 4366–4377, Aug. 2013.

[11] G. C. Sun, "Multi-channel beam steering SAR and GMTIm with high resolution," Ph.D. dissertation, Dept. Elect. Eng., Xidian Univ., Xi'an, China, 2012.

[12] Z. Meng, Y. Li, C. Li, M. Xing, and Z. Bao, "A raw data simulator for bistatic forward-looking high-speed maneuvering-platform SAR," *Signal Process.*, vol. 117, pp. 151–164, Dec. 2015.

[13] Z. Meng, Y. Li, M. Xing, and Z. Bao, "Imaging method for the extended scene of missile-borne bistatic forward-looking SAR," *J. Xidian Univ.*, vol. 43, no. 3, pp. 31–37, Jun. 2016.

[14] S. Chen, Y. Yuan, S. Zhang, H. Zhao, and Y. Chen, "A new imaging algorithm for forward-looking missile-borne bistatic SAR," *IEEE J. Sel. Topics Appl. Earth Observ. Remote Sens.*, vol. 9, no. 4, pp. 1543–1552, Apr. 2016.

[15] L. Zeng, Y. Liang, M. Xing, Y. Huai, and Z. Li, "A novel motion compensation approach for airborne spotlight SAR of high-resolution and high-squint mode," *IEEE Geosci. Remote Sens. Lett.*, vol. 13, no. 3, pp. 429–433, Mar. 2016.

[16] H.-C. Zeng, P.-B. Wang, J. Chen, W. Liu, L. Ge, and W. Yang, "A novel general imaging formation algorithm for GNSS-based bistatic SAR," *Sensors*, vol. 16, no. 3, p. 294, Feb. 2016.

[17] D. Li, W. Wang, H. Liu, H. Cao, and H. Lin, "Focusing highly squinted azimuth variant bistatic SAR," *IEEE Trans. Aerosp. Electron. Syst.*, vol. 52, no. 6, pp. 2715–2730, Dec. 2017.

[18] H. Zhong, S. Zhang, J. Hu, and M. Sun, "Focusing high-squint and large-baseline one-stationary bistatic SAR data using keystone transform and enhanced nonlinear chirp scaling based on an ellipse model," *EURASIP J. Adv. Signal Process.*, vol. 2017, no. 1, pp. 33–45, Dec. 2017.

[19] Y. Li, Z. Zhang, M. Xing, and Z. Bao, "Bistatic spotlight SAR processing using the frequency-scaling algorithm," *IEEE Geosci. Remote Sens. Lett.*, vol. 5, no. 1, pp. 48–52, Jan. 2008.

[20] B. D. Rigling and R. L. Moses, "Polar format algorithm for bistatic SAR," *IEEE Trans. Aerosp. Electron. Syst.*, vol. 40, no. 4, pp. 1147–1159, Oct. 2004.

[21] J. Sun, S. Mao, G. Wang, and W. Hong, "Polar format algorithm for spotlight bistatic SAR with arbitrary geometry configuration," *Prog. Electromagn. Res.*, vol. 103, no. 4, pp. 323–338, 2010.

[22] X. Wang, D. Zhu, X. Mao, and Z. Zhu, "Space-variant filtering for wavefront curvature correction in polar formatted bistatic SAR image," *IEEE Trans. Aerosp. Electron. Syst.*, vol. 48, no. 2, pp. 940–950, Apr. 2012.

[23] S. Tang, "Study on imaging methods for SAR on curved-path platforms," Ph.D. dissertation, Dept. Elect. Eng., Xidian Univ., Xi'an, China, 2016.

[24] H. Deng, Y. Li, M. Liu, H. Mei, and Y. Quan, "A space-variant phase filtering imaging algorithm for missile-borne BiSAR with arbitrary configuration and curved track," *IEEE Sensors J.*, vol. 18, no. 8, pp. 3311–3326, Jan. 2018.

[25] Y. Wu, "Study on multi-mode SAR imaging algorithm and parameter estimation method," Ph.D. dissertation, Dept. Elect. Eng., Xidian Univ., Xi'an, China, 2014.

[26] Z. Li *et al.*, "A frequency-domain imaging algorithm for highly squinted SAR mounted on maneuvering platforms with nonlinear trajectory," *IEEE Trans. Geosci. Remote Sens.*, vol. 54, no. 7, pp. 4023–4038, Jul. 2016.
[27] S. Tang, L. Zhang, P. Guo, G. Liu, and G. C. Sun, "Acceleration model analyses and imaging algorithm for highly squinted airborne spotlight-mode SAR with maneuvers," *IEEE J. Sel. Topics Appl. Earth Observ. Remote Sens.*, vol. 8, no. 3, pp. 1120–1131, Mar. 2015.
[28] Z. Li, Y. Liang, M. Xing, Y. Huai, L. Zeng, and Z. Bao, "Focusing of highly squinted SAR data with frequency nonlinear chirp scaling," *IEEE Geosci. Remote Sens. Lett.*, vol. 13, no. 1, pp. 23–27, Jan. 2016.
[29] Z. Li *et al.*, "A modified equivalent range model and wavenumber-domain imaging approach for high-resolution-high-squint SAR with curved trajectory," *IEEE Trans. Geosci. Remote Sens.*, vol. 55, no. 7, pp. 3721–3734, Jul. 2017.
[30] Z. Meng, "System characteristic and imaging algorithm study on bistatic forward-looking high-speed maneuvering-platform SAR," Ph.D. dissertation, Dept. Elect. Eng., Xidian Univ., Xi'an, China, 2016.
[31] W. Xia, J. Zhu, and J. Zhou, "A raw signal simulator for the side-looking bistatic SAR," in *Proc. ISAPE*, Kunming, China, Nov. 2008, pp. 1266–1269.
[32] W. Xia and J. Zhou, "A raw signal simulator for the squint mode bistatic SAR," in *Proc. ICSP*, Beijing, China, Oct. 2008, pp. 2275–2278.
[33] F. Gao, F. Ma, J. Wang, J. Sun, E. Yang, and H. Zhou, "Visual saliency modeling for river detection in high-resolution SAR imagery," *IEEE Access*, vol. 6, pp. 1000–1014, Nov. 2017.
[34] M. D. Buhari, G. Y. Tian, R. Tiwari, and A. H. Muqaibel, "Multicarrier SAR image reconstruction using integrated MUSIC-LSE algorithm," *IEEE Access*, vol. 6, pp. 22827–22838, Mar. 2018.

SHIYANG TANG (M'16) was born in Jiangsu, China. He received the B.S. and Ph.D. degrees in electrical engineering from Xidian University, Xi'an, China, in 2011 and 2016, respectively. He is currently a Post-Doctoral Researcher with the National Laboratory of Radar Signal Processing, Xidian University. His research interests include imaging of synthetic aperture radar with curved path and high-speed moving target detection and imaging.

HUAN DENG was born in Nanchang, Jiangxi, China, in 1991. He received the B.S degree in communication engineering from Nanchang University, Jiangxi, China, in 2013. He is currently pursuing the Ph.D. degree in signal processing with the National Laboratory of Radar Signal Processing. His research interests include synthetic aperture radar imaging and radar positioning.

PING GUO received the B.S. and Ph.D. degrees in electrical engineering from Xidian University, Xi'an, China, in 2013 and 2017, respectively. She is currently with the College of Communication and Information Engineering, Xi'an University of Science and Technology. Her research interests include imaging of several synthetic aperture radar modes, and moving target detection and imaging.

YACHAO LI was born in Jiangxi, China, in 1981. He received the M.S. and Ph.D. degrees in electrical engineering from Xidian University, Xi'an, China, in 2005 and 2008, respectively. He is currently a Professor with Xidian University. His research interests include synthetic aperture radar (SAR)/ISAR imaging, missile-borne SAR imaging, ground moving target indication, matching and orientation of SAR image, real-time signal processing based on field-programmable gate array and DSP technology, and distributed radar.

LINRANG ZHANG was born in Shaanxi, China, in 1966. He received the M.S. and Ph.D. degrees in electrical engineering from Xidian University, Xi'an, China, in 1991 and 1999, respectively. He is currently a Full Professor with the National Laboratory of Radar Signal Processing, Xidian University. He has authored or co-authored three books and published over 100 papers. His research interests include radar system analysis and simulation, radar signal processing, and jamming suppression.